Journal of Maps

ISSN: (Print) 1744-5647 (Online) Journal homepage: http://www.tandfonline.com/loi/tjom20

Fluvial-aeolian sedimentary facies, Sossusvlei, Namib Desert

Amelie Feder, Robert Zimmermann, Harald Stollhofen, Luca Caracciolo, Eduardo Garzanti & Louis Andreani

To cite this article: Amelie Feder, Robert Zimmermann, Harald Stollhofen, Luca Caracciolo, Eduardo Garzanti & Louis Andreani (2018) Fluvial-aeolian sedimentary facies, Sossusvlei, Namib Desert, Journal of Maps, 14:2, 630-643, DOI: 10.1080/17445647.2018.1526719

To link to this article: https://doi.org/10.1080/17445647.2018.1526719

JOURNAL OF MAPS
2018, VOL. 14, NO. 2, 630–643
https://doi.org/10.1080/17445647.2018.1526719

Taylor & Francis
Taylor & Francis Group

Science

Fluvial-aeolian sedimentary facies, Sossusvlei, Namib Desert

Amelie Feder[a], Robert Zimmermann [b], Harald Stollhofen [a], Luca Caracciolo [a], Eduardo Garzanti [c] and Louis Andreani [b]

[a]GeoZentrum Nordbayern, Friedrich-Alexander-University (FAU) Erlangen-Nürnberg, Erlangen, Germany; [b]Division 'Exploration Technology', Helmholtz-Zentrum Dresden-Rossendorf, Helmholtz Institute Freiberg for Resource Technology, Freiberg, Germany; [c]Laboratory for Provenance Studies, Department of Earth and Environmental Sciences, University of Milano-Bicocca, Milano, Italy

ABSTRACT

Aeolian sedimentary processes and corresponding facies shape the Earth's surface and control the evolution of dune fields. The Namib Sand Sea with its Sossusvlei playa-lake is a perfect example to investigate the spatial distribution of fluvially influenced aeolian deposits. Remote sensing in combination with ground observations allowed for mapping of the facies distribution pattern of associated fluvial and aeolian sediments. Laboratory spectral signature measurements were used to further improve the separation between six groups of facies: modern aeolian sand, deflation surface, mud pool/mud drapes, heavy mineral lag, reworked fluvial–aeolian sediments, and fossil dune remnant. The best results were achieved through a supervised classification algorithm trained by field observations, a combination of Principal Component Analysis, band ratios, texture and geomorphologic indices. Consequently, a map outlining the facies distribution pattern of the Sossusvlei area at a scale of 1:10,000 was created. We propose this as a possible workflow to efficiently map and monitor desert environments and to investigate the interplay of aeolian and fluvial sediments.

ARTICLE HISTORY
Received 17 April 2018
Revised 10 September 2018
Accepted 11 September 2018

KEYWORDS
Sossus sand formation; world view 3; dune river interaction; modern sediments; facies mapping; Quaternary

1. Introduction

Remote sensing is a valuable tool for lithological mapping of remote or inaccessible areas. In the last decade, it has been successfully applied for mineral mapping and exploration of different terrains using various sensor combinations (Bertoldi et al., 2011; Bullard, White, & Livingstone, 2011b; Sabins, 1999; van der Meer et al., 2012; Zimmermann, Brandmeier, Andreani, Mhopjeni, & Gloaguen, 2016). This technique has also been used to investigate the geology and geomorphology of other planets, including Mars (Parker, Gorsline, Saunders, Pieri, & Schneeberger, 1993), Mercury (Stepinski, Collier, McGovern, & Clifford, 2004) and Pluto (Telfer et al., 2018).

In the Namib Desert, numerous remote sensing studies have been conducted over the last decades (Livingstone, 2013). Over this time, the technical possibilities of remote sensing have improved and the extracted information has increased in quality and quantity. Strohbach (2008) created a catchment map on the main rivers in Namibia with Shuttle Radar Topography Mission-Digital Elevation Model (SRTM-DEM) data and White, Walden, and Gurney (2007) investigated changes in dune colour and iron oxide content. The morphometry of dunes was investigated focusing on their height, spacing and thickness of the sand (Blumberg, 2006; Bullard, White, & Livingstone, 2011a; Lancaster, 1989) and the distribution of dune types, which have been mapped extensively (Besler, 1980; Breed et al., 1979; Livingstone et al., 2010). However, a detailed map of sedimentological facies is still missing. Overall, attempts to map the spatial distribution of sedimentary facies with remote sensing are very scarce (Castañeda, Herrero, & Casterad, 2005; Maeder et al., 2002; Quintanar, Khan, Fathy, & Zalat, 2013; Raines, Offield, & Santos, 1978). This paper aims at testing the applicability of remote sensing of facies in a sand desert environment. It is specifically focused at mapping and constraining the interaction between aeolian and ephemeral fluvial processes, as they are the main force for the generation of facies and the geomorphological shaping.

In recent years, the topic of aeolian and fluvial interaction in dryland environments has gained traction. The studies investigated controlling factors, different interaction types and geomorphological landforms (Al-Masrahy & Mountney, 2015; Bullard & Livingstone, 2002; Liu & Coulthard, 2015; Roskin, Bookman, Friesem, & Vardi, 2017). It is understood that fluvial–aeolian interaction is crucial for the evolution of

CONTACT Amelie Feder amelie.troidl@gmail.com GeoZentrum Nordbayern, Friedrich-Alexander-University (FAU) Erlangen-Nürnberg, Erlangen, Germany

Supplemental data for this article can be accessed at https://doi.org/10.1080/17445647.2018.1526719.

Figure 1. Location of the Namib Desert (shown in orange), the erg 'Namib Sand Sea' (shown in yellow) and the study area around Sossusvlei (modified after Livingstone, 2013)

dune fields and that aeolian sediments may be mainly preserved by fluvial interactions in inter-dune areas (Fryberger, Krystinik, & Schenk, 1990). This paper focuses on the interplay of these two processes especially on the resulting facies and their spatial distribution and mixing of fluvial and aeolian sediments.

The Sossusvlei playa-lake system is located at the eastern flank of the Namib Sand Sea (*sensu* Lancaster, 1985) in central Namibia (Figure 1). It provides an excellent example of sedimentological processes associated with an ephemeral river repeatedly entering a dune field, becoming dammed and finally terminating in a flat inter-dune playa called '*vlei*'. The spectrum of aeolian and fluvial processes generates a complex interplay of sedimentary facies, which make a facies map a prerequisite to better understand the mutual relationships and distribution pattern of the sediments. The Namib Sand Sea is perfectly suited for remote sensing as there is little vegetation, rare cloud coverage and restricted anthropogenic modification due to its setting in a protected national park area.

Data from the Worldview 3 platform are used because of its high-spatial resolution as well as their band combination, making them particularly suitable for geological analysis (Kruse, Baugh, & Perry, 2015; Kruse & Perry, 2013; Ye, Tian, Ge, & Sun, 2017). This approach highlights compositional differences on an m-scale, with notably greater detail compared to other satellite systems (e.g. Advanced Spaceborne Thermal Emission and Reflection Radiometer (ASTER)). Such a high resolution is critical for sedimentological studies as they allow consideration of small-scale morphological features associated with sediment surfaces.

2. Namib Desert and Namib Sand Sea

The Namib Sand Sea is part of the Namib Desert in central southern Namibia (Figure 1). It stretches from the ephemeral Kuiseb River in the north to Lüderitz in the south (Ward, 1988) and extends for up to 140 km inland (White et al., 2007). It contains

a broad variety of different dune shapes: large linear dunes, star-shaped dunes, simple and compound transverse, barchanoid dunes, coppice dunes and sand-ramps (Lancaster, 2014; Miller & Becker, 2008; Rowell et al., 2018; Stone, 2013).

Climatic conditions in the area have remained hyper arid since the Miocene (Lancaster, 2002). The convergence of the warm Angola Current with the cold Benguela Current and subtropical high-pressure systems cause low humidity and only limited precipitation (ranging between ~ <50 mm/yr at the coast to ~100 mm/yr near the escarpment) between c. 30 and 15°S (Garzanti et al., 2017; Lass, Schmidt, Mohrholz, & Nausch, 2000; Shannon & Nelson, 1996). Vegetation is very limited and critically depends on frequent fogs (Eckardt et al., 2013). Strong southerly winds prevail, except during winter when the so-called *Berg Winds* occasionally blow from the north-east (Lancaster, 1985).

Except for the Orange and the Kunene, all Namibian rivers are ephemeral (Krapf, Stollhofen, & Stanistreet, 2003) with the majority of them draining west towards the Atlantic. Catchments start 100–300 km east of the coastline, where mean annual rainfall is about 300–500 mm (Jacobson, Jacobson, & Seely, 1995). Minor river activity occurs almost annually, but major flooding events (Stanistreet & Stollhofen, 2002) are restricted to climatic disturbances, such those related to El Niño that cause a southward shift of the intertropical convergence zone, and produce exceptional rainfall (Shannon, Boyd, Brundrit, & Taunton-Clark, 1986).

Sand-sized sediments transported by the Orange River to the Atlantic Ocean are displaced northward by powerful and persistent longshore currents to reach as far north as Namibe city in Angola (Garzanti et al., 2015; Garzanti et al., 2017). In southern Namibia, they are blown out from modern and palaeo-beaches and accumulate in the Namib Sand Sea, which, therefore, represents the wave- and wind-displaced part of the Orange River Delta (Garzanti et al., 2012; Rogers, 1977).

2.1. Geological setting of the study area

The geological map of the area, Sheet 2414 – Meob Bay at the scale 1:2,50,000 (Richards, Schreiber, Tjikukutu, & Cloete, 2000) shows the distribution of Neoproterozoic, Palaeozoic, and Cenozoic units, and divides the Quaternary units of the Sossusvlei region into 'alluvium', 'undifferentiated sand, gravel, calcrete', and the 'Sossus Sand Formation'. The analysed samples originate in the alluvium and Sossus Sand Formation.

The study area encompasses the modern dune, river and playa-lake environments of Sossusvlei and Deadvlei which form at the end of the Tsauchab River (Figure 1). The Tsauchab River has an approximate length of 150 km, with a catchment area of about 4000 km², and largely drains the Naukluft Mountains (Jacobson et al., 1995). The catchment comprises a variety of Neoproterozoic to Cambrian rocks, including quartzite, shale, limestone, dolomite, porphyry, granite, and gneiss (Villers et al., 1964).

The river flows across an extensive deflation plain and deeply penetrates the eastern flank of the sand sea for c. 40 km to terminate eventually at Sossusvlei. Water reaches the vlei only every few years (Brook, Srivastava, & Marais, 2006). Sparse vegetation grows along the river pathway and around the vlei where groundwater is available. Deflation surfaces – some including thin mud drapes and occasional thin aeolian sand sheets – are found at the dune entry point along the river valley.

The river carries mud, silt, sand, and fine gravel. Coarser-grained bedload stays in the river channels whilst thin mud drapes form along the thalweg during the waning stages of occasional floods. Thicker accumulations of mud settle in variably sized interdune pools such as the Sossusvlei. Because of the ephemeral nature of the river, the mud pools/drapes dry out rapidly forming spectacular mud cracks. Semi-consolidated 'fossil' aeolian sandstones crop out at the margin of the vlei, infiltrated by mud and also often sealed by a thin mud layer, largely protecting them from aeolian erosion (Krapf et al., 2003).

The larger Deadvlei and other mud pool relicts are located south and southeast of Sossusvlei and represent older terminal lakes of the Tsauchab River. Sediments of the Deadvlei were deposited at about 0.9–0.3 ka B.P. during a period of higher fluvial activity (Brook et al., 2006). In the area between Sossusvlei and Deadvlei, along the main tracks to the vleis, the thin mud drapes are mostly destroyed and mixed with aeolian sand by the trampling of tourists.

Adjacent to the Sossus and Deadvlei areas, a multidirectional wind regime favours the formation of complex star dunes with heights reaching 300–360 m and widths of 400–500 m (Lancaster & Teller, 1988; Livingstone et al., 2010). In areas of fluvio-aeolian interaction and/or lower wind velocity, other aeolian deposits such as sand sheets, sand ramps, barchan and coppice dunes prevail.

3. Data and methods

Worldview-3 (WV-3) is a multispectral satellite system covering the Earth's surface in 29 spectral bands (Table 1). A package of four visible to near-infrared (VNIR; blue, green, red, near-infrared (NIR 1)) and eight short wave infra-red (SWIR) bands are used in this study. The scene was preprocessed by Digital Globe to the ortho-rectified standard level 2A.

The scene was recorded on 29.04.2015 at 09:20:53 UTC with no cloud cover.

Table 1. Technical Data Worldview 3 (Digital Globe).

Orbit	Altitude: 617 km Type: SunSync, 1:30 pm descending Node Period: 97 min.
Sensor Bands	Panchromatic: 450–800 nm 8 Multispectral: Red: 630–690 nm Blue: 450–510 nm Green: 510–580 nm Near-IR1: 770–895 nm 8 SWIR Bands: SWIR-1: 1195–1225 nm SWIR-5: 2145–2185 nm SWIR-2: 1550–1590 nm SWIR-6: 2185–2225 nm SWIR-3: 1640–1680 nm SWIR-7: 2235–2285 nm SWIR-4: 1710–1750 nm SWIR-8: 2295–2365 nm
Sensor Resolution	Panchromatic Nadir: 0.31 m 20° Off-Nadir: 0.34 m Multispectral Nadir: 1.24 m 20° Off-Nadir: 1.38 m SWIR Nadir: 3.70 m 20° Off-Nadir: 4.10 m
Dynamic Range	11-bits per pixel Pan and MS; 14-bits per pixel SWIR

Worldview-3 was chosen over other available datasets because the high-spatial resolution (~4 times better than ASTER or Landsat) enables the delineation of confined exposures of single facies. Furthermore, due to the spectral resolution in the SWIR (8 channels compared to the 6 of ASTER and the 2 of Landsat), facies can be separated by means of their clay and carbonate contents.

An ALOS PALSAR [Dataset: © JAXA/METI ALOS PALSAR ALPSRP0554066802007. Accessed through ASF DAAC 11 October 2017] DEM was used to calculate geomorphological derivates. The DEM has a resolution of 15 m and an estimated accuracy of 2.5 m (Rosenqvist, Shimada, & Watanabe, 2004). Geomorphological indices like the Topographic Position Index (TPI) and slope were calculated using the TecGEM toolbox (Andreani, Stanek, Gloaguen, Krentz, & Domínguez-González, 2014) for landform analysis.

Laboratory spectral measurements of representative soil samples were performed to evaluate the spectral separability of the sedimentary facies (for description of samples see section 'Ground Truthing'). A Spectral Evolution PSR-3500 portable spectroradiometer was used to record the spectra in the wavelength range between 400 and 2500 nm (VNIR to SWIR). Spectral data were acquired using a contact probe with constant illumination and a spot size of 8 mm. The spectral readings were calibrated against a calibrated Polytetrafluoroethylene (PTFE) panel with >99% reflectance in VNIR and >95% in SWIR. Eight spots were measured and averaged per sample to account for heterogeneities.

3.1. Pre-processing

Pre-processing follows the workflow outlined by Kuester (2016) (Figure 2) and starts with converting digital numbers (DN) to at-sensor radiance and then calculating the top of the atmosphere (TOA) reflectance. The

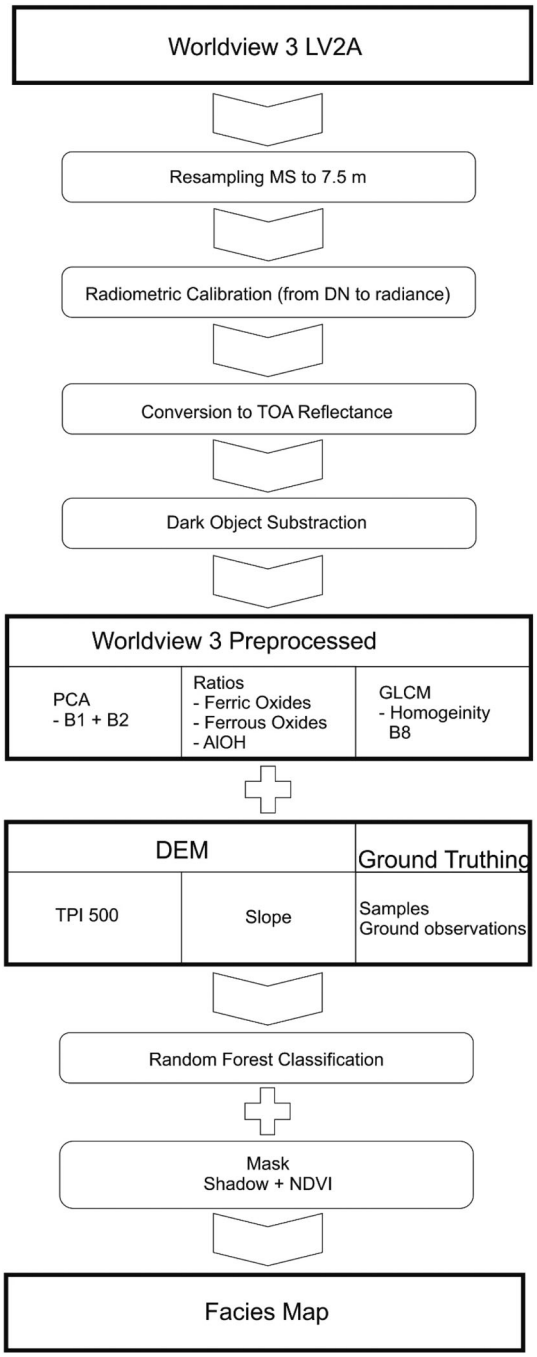

Figure 2. Workflow for pre-processing and classification of the Worldview 3 image.

VNIR bands (bands 1–4) are resampled to match spatial resolution of the SWIR bands using a nearest neighbour algorithm. Effects of atmospheric scattering are removed using a dark object subtraction (Chavez, 1988).

Furthermore, a composite mask as proposed by various authors was applied:

(1) A Normalised Difference Vegetation Index (NDVI) mask was calculated. A threshold value of 0.21 was applied to mask out pixels associated with vegetation based on the results of Gitelson and Merzlyak (1994). NDVI values of greater than 0.2

is usually referred to increasing chlorophyll content of vegetation (van der Meer et al., 2000).

(2) low albedo pixels with a reflection <5% in the SWIR-4 band (at 1735 nm) were masked because of strong shadows at the western side of the dunes caused by scene acquisition in the early morning.

3.2. Processing

Following pre-processing, several analyses were applied to both the multispectral satellite image and the DEM. Dimensionality reduction and noise filtering were performed using Principal Components Analysis (PCA) to reduce linearity effects between the 12 WV-3 bands (Gomez, Delacourt, Allemand, Ledru, & Wackerle, 2005). Band ratios such as those for clays or iron were deployed in order to discriminate different mineralogical compositions (Amer, Kusky, & Ghulam, 2010; Elsayed Zeinelabdein & Albiely, 2008; Gad & Kusky, 2007; Rowan & Mars, 2003; van der Meer et al., 2012). They are used to enhance spectral differences – based on the mineralogy – by dividing specific spectral bands by each other in order to see the relative band intensities.

Texture statistics are derived from a Gray Level Co-Occurrence Matrix (GLCM) (Barber & LeDrew, 1991) applied on the WV-3 dataset. The GLCM algorithm calculates how often pixel with specific gray-level and a fixed spatial distance and angle occur (Haralick, Shanmugam, & Dinstein, 1973). Several statistical parameters can be derived from this matrix. It is well suited to classify by means of diversity of neighbouring pixels. The TPI highlights differences in elevation between the average elevation *zi* and the central pixel *z0* within a predefined radius *R* (Gallant & Wilson, 2000). Best results for the study area were achieved using a moving window width (2*R) of 33 pixels (500 m), roughly corresponding to the width of the largest dunes. Furthermore, a standard slope map was calculated.

Different composite images of PCA + Band-ratios + Homogeneity + TPI + slope are fed into the classification and are validated with the field data. The random forest classification (Breiman, 2001) was chosen because of its high suitability for remote sensing (Cracknell & Reading, 2014). Compared to other machine-learning algorithms, it is easily trained, works reliably under a variety of input parameters and classifies accurately even with scattered training data (Cracknell & Reading, 2014). All processing is conducted in R language (R Core Team, 2016) using the packages raster (Hijmans, 2017), rgdal (Bivand et al., 2017), glcm (Zvoleff, 2016) and randomForest (Liaw, Wiener, Breiman, & Cutler, 2015).

3.3. Ground truthing

Sampling and validation campaigns in 2016 and 2017 were based on a preliminary interpretation of satellite images. Data on sedimentary structures, grain sizes and compositional characteristics of the different facies were collected in detail in the field. Representative samples from each facies were taken around Sossusvlei and Deadvlei, additional ground observations and extensive photo documentation were logged using a handheld GPS.

Accordingly, the following six sedimentary facies were distinguished and characterized (see Table 2): (I) modern aeolian sand (Figure 3(A); including dune and sheet sands), (II) deflation surface (Figure 3(B); including interdune wind corridors, windward inclined sandramps, deflationary sand sheets, deflation plains), III) mud pool/mud drapes (Figure 3 (C)), (IV) heavy mineral lag (Figure 3(D)), (V) fluvial–aeolian reworked (Figure 3(E)), and (VI) fossil dune remnant (Figure 3(F)). It should be noted that, apart from localized thin mud drapes, no *in situ* fluvial deposits are currently exposed at the surface, due to intense aeolian deflation, reworking and/or aeolian sand coverage. Deposited sand and gravel fractions in fluvial facies are, in fact, modified by intense aeolian activity, resulting in well-developed deflation surfaces and fluvial–aeolian reworked facies type.

4. Results and discussion

4.1. Spectroscopic analysis of representative samples

Spectra of mud pool and heavy mineral lag are easy to discriminate from the surrounding facies. The spectral measurements for the remaining facies (Figure 3) display only slight differences in shape and location of their absorption minima (Table 3, Figure 4). Thus, additional data (like geomorphologic and textural analysis) are, therefore, needed to successfully discriminate among them.

The high Fe^{2+}/Fe^{3+} charge-transfer absorption (Hunt, 1977) in modern aeolian sand, deflation surface, fossil dune remnants, and fluvial–aeolian reworked sediment originate from iron-rich coatings formed around the aeolian sand grains (Walden, White, & Drakes, 1996; White et al., 2007). In general, the Fe^{2+}/Fe^{3+} absorption minima is located around 910 nm, indicative at goethite-rich coatings (Hunt, 1977). However, for the heavy mineral lag the Fe^{2+}/Fe^{3+} feature is shifted towards a lower wavelength, indicating more hematite-rich constituents (Hunt, 1977).

In all samples, the Al–OH overtone vibrational feature is shifted towards a higher wavelength, indicating Al-poor compositions (Cudahy et al., 2008). Deepest absorption, and thus highest clay content, shows the samples of mud pool/drape, followed by fossil dune remnants and deflation surfaces. Mud pool/drape

Table 2. Field description of sedimentary facies occurring in Sossusvlei. They were recorded during the field campaigns 2016 and 2018.

Facies	Map colour	Sediment colour	Sediment surface	Grainsize	Sediment structures	Compositional characteristics	Vegetation	Occurrence
Modern aeolian sand	Yellow	Pale red	Semi-horizontal to steeply inclined <35°	Medium-grained sand (well sorted)	Grain flow lobes on lee side, wind rippled surfaces on stoss side	Dominantly quartz, few feldspar and lithics	Grasses in flatter terrain; bushes assocd. with coppice dunes	Dunes, interdune sheet sands, downwind elongated coppice dunes
Deflation surface	Orange	Grey	Planar to slightly inclined <10°, slightly undulating	Medium to coarse-grained sand with granules	Granule rippled surfaces	Quartz, lithics, including carbonates	Occasional shrubs or grass	Interdune areas, deflation surfaces, deflationary sand sheets and windward inclined sand ramps
Mud pool and mud drapes	Light blue	Beige	Subhorizontal, subplanar	Mud, silt, occasionally with admixed aeolian sand	Plane bedded, polygonal desiccation cracks, infilled with aeolian sand, rain drop imprints, some burrowing	Clay minerals, quartz, minor calcite	Almost absent in central parts, but frequent in areas fringing pools	Terminal lake (vlei) deposits in interdune lows, mud drapes along river Thalweg and in overbank areas
Heavy mineral lag	Red	Dark reddish-brown	Moderately to steeply inclined <35°	Fine to medium sand	Granule rippled surfaces	Quartz, feldspar, lithics; frequent heavy mineral enrichments	Absent	Windward dune and coppice dune flanks
Fluvial–aeolian reworked	Green	Reddish-beige	Semi-horizontal to moderately inclined <15°, rough surfaces	Poorly sorted occ. bimodal mixture of medium-grained sand with granules and mud chips	Wind ripples, thin mud drapes in elongated channel depressions (Thalweg)	Dominantly quartz, few feldspar and lithics, mud chips/curls layer-wise concentrated	Absent	Aeolian reworked fluvial sands in elongate channel depressions; aeolian accumulation in interdune wind corridors and at windward dune bases
Fossil dune remnant	Rose	Orange	Moderately to steeply inclined <35°, undulatory	Medium-grained sand with some infiltrated mud	Cross-stratified, in places burrowed, occasional fossil roots	Quartz, feldspar, clay	Absent to rare	Semi-lithified dunes, preferentially in marginal vlei areas

consists mainly of clay minerals and the other facies contain mud chips and clasts.

The samples from deflation surfaces show exclusively a notable carbonate absorption feature around 2337 nm, indicative of calcite (Zaini, van der Meer, & van der Werff, 2014). Carbonate clasts were originally carried by the river (Jacobson et al., 1995) and accumulate on deflation surfaces and deflationary sand sheets due to their relative coarse grain sizes. Other sources for carbonate are aeolian dust drapes, sourced from deflated calcrete surfaces exposed towards the east of the vlei area, at the foot of the escarpment.

4.2. Remote sensing analysis

Several approaches have been tested in order to differentiate the sedimentary facies exposed in the Sossusvlei area. The processing workflow was optimized to maximize the interpretative potential. Based on the eigenvalues, the two first PCA components explain more than 98% of the variability, and are therefore sufficient for a robust classification. Three main groups can already be identified from the RBG false colour image of PCA band 1, 2, and 3 (Figure 5(a)): (1) mud pools/mud drapes in white/light green, (2) modern aeolian sand in pink/cyan, and (3) deflation surfaces in green. However, the heavy mineral lag, the fluvial–aeolian reworked facies, and the fossil dune remnants do not show distinctive patterns.

Band ratios based on the results of spectral analysis are further included into the classification. Best results are obtained for ferric oxides (SWIR3/NIR1), ferrous iron [(SWIR5/NIR1)+(Green/Red)], and AlOH abundance [(SWIR5 + SWIR8)/SWIR6] (Henrich, Krauss, Götze, & Sandow, 2017). Ferrous iron is mainly concentrated in the mud pools/mud drapes (Figure 5(b)). The results for the ferric oxide band ratio confirmed previous observations by White et al. (2007), showing that Fe^{3+} abundance is highest in sand dunes located 80–90 km inland from the coast. Figure 5(c) shows that modern aeolian sand and fossil dune remnant facies have the highest ferric oxide abundance, whereas heavy mineral lag and mud pool/mud drapes facies have the lowest. The highest Al–OH ratio is displayed for mud pool/drape facies (Figure 5(d)). All three ratios for deflation surface and the reworked aeolian facies range between those of the mud pool/mud drape and modern aeolian sand.

The similarities in mineralogical composition (revealed by the spectral data and ground-truthing) and the morphologic differences in areas covered by different facies, support the need for including geomorphologic analysis (of slope, TPI and textural analysis) as additional classification layers. Despite similar mineralogical compositions (revealed by the spectral data and ground-truthing), sedimentary

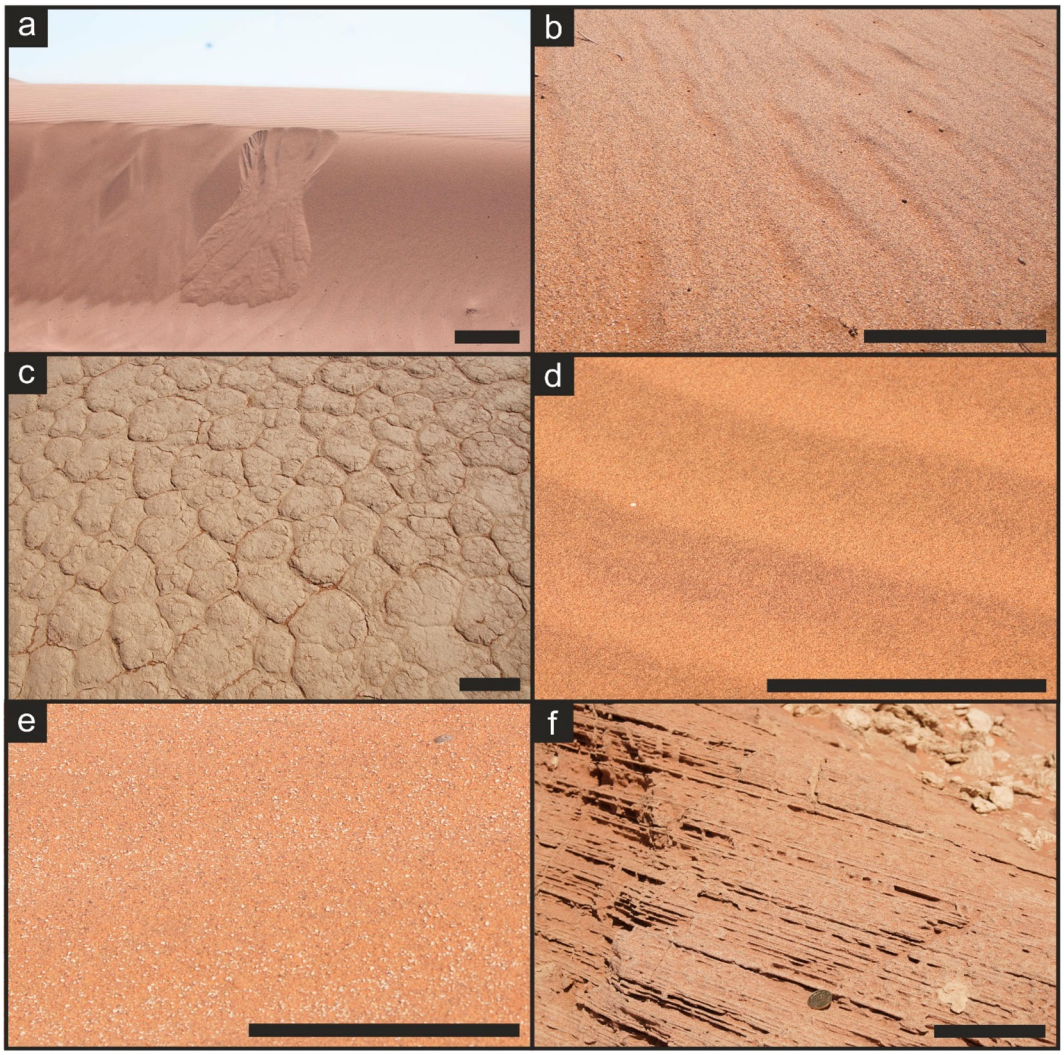

Figure 3. Photographs of the different facies identified in the field (Black bar for scale = 20 cm). (a) Modern aeolian sand (small dune with grain flow lobes); (b) deflation surface with granule rippled surface; (c) mud pool with polygonal desiccation cracks; (d) heavy mineral lag (e) fluvial–aeolian reworked facies, comprising aeolian sand and mudchips; and (f) fossil dune remnant showing crossbeds.

facies, exert a primary control on both geomorphological (of slope, TPI and textural analysis) and textural indices (homogeneity). Thus geomorphological indices can be successfully used for discrimination and improving classification accuracy. Geomorphological indices distinguish between steep dune sand and sub-horizontal mud pools/mud drape surfaces. The fluvially aeolian reworked facies as well as defation surfaces are associated with slightly inclined surfaces within the dunes, whereas heavy mineral lags occur on steeper surfaces. Deflation surfaces build on either flat interdune areas or on the slightly inclined base of the dunes.

Textural analysis (homogeneity) based on SWIR 8 band allows distinguishing fossil dune remnants and the reworked aeolian facies from other facies. Homogeneity is, in this case, the most meaningful parameter as the two above mentioned facies show a low homogeneity due to more variable composition.

Based on the above observations, the input file for classification includes: (1) the first two PCA components; (2) three-band ratios; (3 and 4) TPI and

Table 3. Absorption wavelength and depth calculated from mean spectra of the respective lithological units for the $Fe^{2+/3+}$, AlOH and carbonate absorption features.

	Fe^{2+}/Fe^{3+} Abs Wvl	Depth	Al–OH Abs Wvl	Depth	Carbonate Abs Wvl	Depth
Modern aeolian.sand	905	0.031	2206	0.016	2335	0.001
Deflation surface	911	0.040	2206	0.018	2337	0.009
Mud pool	907	0.023	2208	0.020	2339	0.002
Heavy Mineral lag	894	0.008	2206	0.011	2335	0.004
Fluvial–aeolian reworked	910	0.039	2208	0.016	2337	0.002
Fossil dune remnant	908	0.043	2208	0.020	2337	0.003

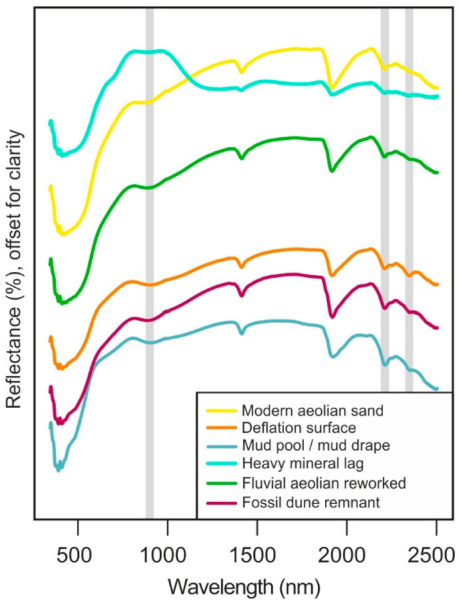

Figure 4. Spectral signatures of the facies. Spectra are offset for clarity. The grey bars indicate the location of absorption minima for Fe^{2+}/Fe^{3+}, Al–OH and CO_3^{2-} respectively.

slope; and (5) homogeneity of SWIR band 8. Calibration points and validation areas were created in QGIS, based on GPS points and samples collected in the field. Using only data based on the spectral input, the classification reached an overall accuracy of 84%. By adding morphometric indices (TPI and slope) and textures (GLCM homogeneity for surface textures) the accuracy could be increased by 7% up to 91% (Table 4). The confusion matrix for classification with the highest accuracy is shown in Table 5. Fluvial–aeolian reworked deposits still show the most significant deviations which can result from the mixing of fluvial and aeolian material. The facies consists of both aeolian sand and fluvial mud chips, the size (2 mm to 5 cm) and the amount of the mud chips vary in different areas.

4.3. Facies mapping

The facies in the Sossusvlei area can be described by means of remote sensing as units with specific spectral, geomorphological and textural characteristics based on training areas. However, limitations are given by spatial resolution of the satellite images (7.5 m) and spectral separability of the sedimentary facies. On the other hand, classical mapping techniques are hardly applicable due to sensitivity and accessibility of the area. Remote sensing proved able to accurately classify areas that can be correlated to modern aeolian sand, mud pool/mud drape, deflation surface, heavy mineral lag, fluvial–aeolian reworked, and fossil dune remnant facies (Table 5 and Figure 5) and to show their detailed areal distribution (Figure 6). Basing on satellite imagery, the Sossus Sand Formation can be therefore further subdivided into modern aeolian sand, heavy mineral lag and dune remnant facies units. The 'Alluvium' is in fact only represented by mud pools/mud drapes and deflation surfaces. Some deflation surfaces in inter-dune areas along and adjacent to the Tsauchab river comprise concentrations of fluvial pebbles in layers. The fluvial–aeolian reworked facies and also many of the deflation surfaces record the interplay of aeolian and fluvial processes. The fluvial–aeolian reworked facies consists of fluvial–aeolian reworked fluvial sand and small mud chips of the 'Alluvium' (waning flood muds deposited along the thalweg) mixed with recycled aeolian sands of the Sossus Sand Formation.

The mud pool/mud drape facies is easily distinguished in both the field and by remote-sensing by its low Fe^{2+}/Fe^{3+} and high AlOH absorption features. The mud pools occupy large, flat inter-dune areas characterized by terminal lake deposits. Deflation surfaces comprise extensive deflation areas in the flat river valley, deflationary sand sheets, and small deflation areas associated with interdune areas and some dune flanks. The discrimination is particularly effective for this facies, because of its unique carbonate absorption. The Sossus Sand Formation includes sand dunes and aeolian sheet sands, and is characterized by low AlOH absorption and deep Fe^{2+}/Fe^{3+} absorption. Heavy mineral lags occupy localized areas of the dunes where heavy minerals are concentrated by aeolian sorting processes and mostly occur in the southern part of the (Main Map). Fossil dune remnants and fluvial–aeolian reworked facies are those with the highest rate of misclassified pixels, due to their intermediate composition between dune sand and mud pool/mud drape. However, classification accuracy is increased if spectral data are integrated with textural and morphological information (Table 4).

Additional facies may be identified in the field, however, they cannot be distinguished through remote-sensed images at the present resolution of 7.5 m. These features might be resolved in future and mapped by a multi- or hyperspectral camera with a decimetre resolution carried on a drone. For the time being, it was not possible to discriminate between fluvial and aeolian sands in the Sossusvlei, because the former mix quickly with the latter after the river enters the desert (Garzanti et al., 2012) and finally become reworked by aeolian activity. As a consequence, samples taken in the entryway to Sossusvlei have a similar spectral signature as modern aeolian sand. Fluvial sands might only be differentiated by collecting samples immediately after extensive flooding and using a satellite image taken from that same time period. However, these periods count as 'events', whereas our map documents the overwhelming dry periods in between major flooding events.

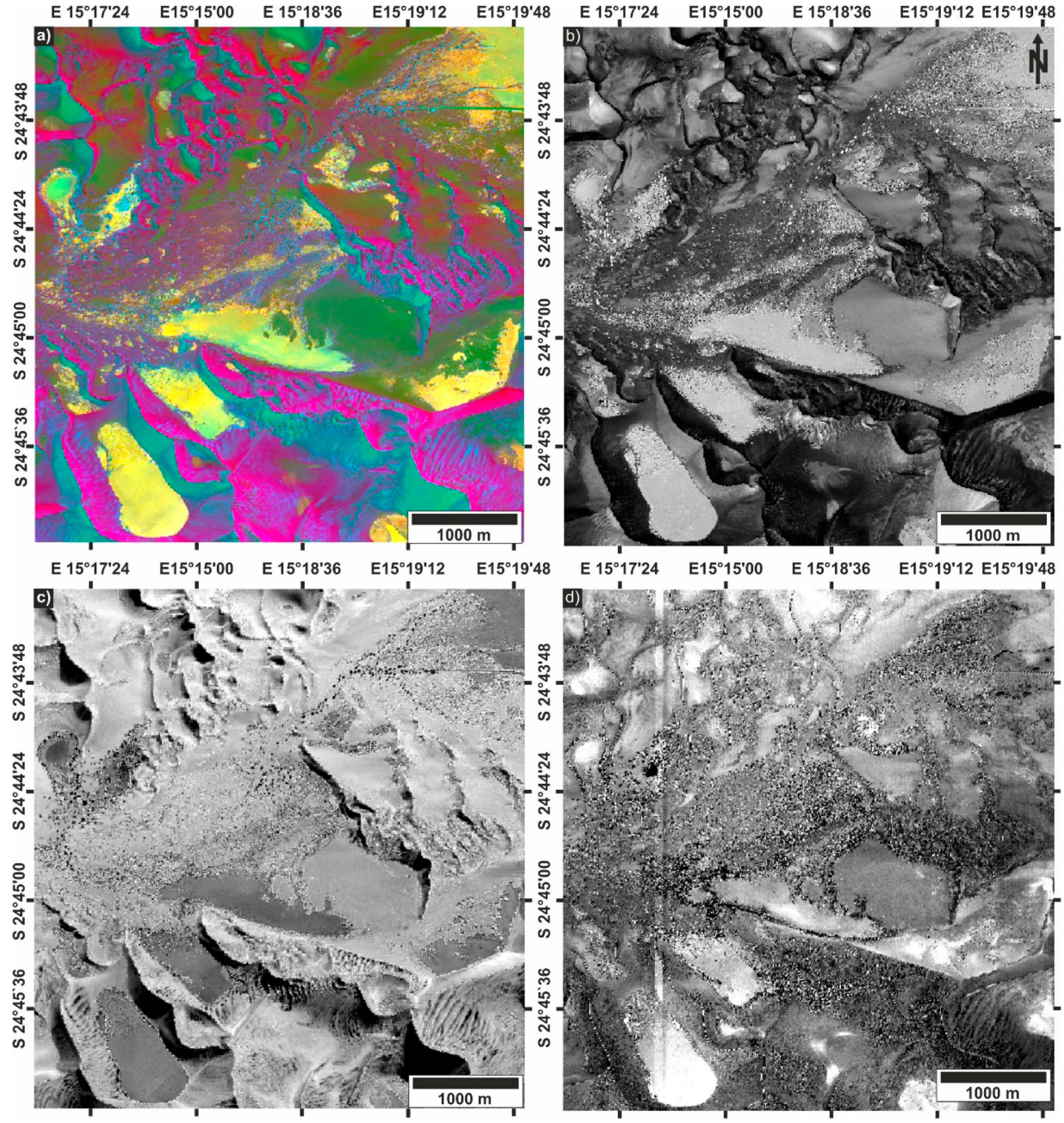

Figure 5. Band ratio images and PCA (lighter colours stand for a high concentration and dark colors for a low concentration). The images have the same extent as the highlighted frame in Figure 1. (a) PCA 1+2+3; (b) Ferrous iron ratio; (c) Ferric Oxides ratio; and (d) Al–OH ratio (Image © 2015 DigitalGlobe, Inc.).

4.4. Fluvial–Aeolian interactions

The (Main Map) shows the interplay of aeolian and fluvial facies (Figure 6). As expected, modern aeolian sand makes up the upper active part of the dunes, and mud pools form in inter-dune areas. After drying out, the mud pools are efficiently eroded by the wind and redeposited on the adjacent slightly to moderately inclined dune flanks as mud curls and chips intermixed with reworked aeolian sediments (fluvial–aeolian reworked).

Coarser fluvial material (deflation surface) is redistributed during events with increased wind energy and accumulates on variably sized deflation surfaces on the slightly inclined dune flanks and inter-dune areas. Smaller grains are removed with only coarse-grained sand and pebbles remaining.

Fossil dune remnants are mainly exposed at the margins of the vleis. They are cemented during floods when mud infiltrated the lower part of the dunes which was

Table 4. Accuracy assessment for different set of input parameters for the supervised Random Forest classification. The overall accuracy highly improves by adding multiple independent datasets.

Input parameters	Overall accuracy (%)
PCA + Ratios	0.84
PCA + Ratios + Geomorphology	0.88
PCA + Ratios + Geomorphology + Texture	0.91

Table 5. Confusion matrix for the Random Forest classification resulting the highest accuracy.

Class	Modern dune sand	Mud pool	Deflation bypass surface	Deflation lag	Fossil dune remnant	Aeolian reworked	Total (%)
Modern dune sand	88	4	0	4	4	0	100
Mud pool	0	100	0	0	0	0	100
Deflation surface	0	0	100	0	0	0	100
Heavy mineral lag	0	0	0	100	0	0	100
Fossil dune remnant	0	0	0	0	100	0	100
Fluvial–aeolian reworked	0	5.6	0	16.7	5.6	72.2	100

covered with water (Langford, 1989). During the next flooding events, the river removes the loose sand leaving the fossil dune remnants exposed.

Localized lag deposits enriched in heavy minerals accumulate on dune flanks, coppice dunes and larger sand ripples because of selective-entrainment processes (Garzanti et al., 2015). In the remote-sensed map, only the larger accumulations on dune flanks are visible, while the other ones are spatially too small to be resolved.

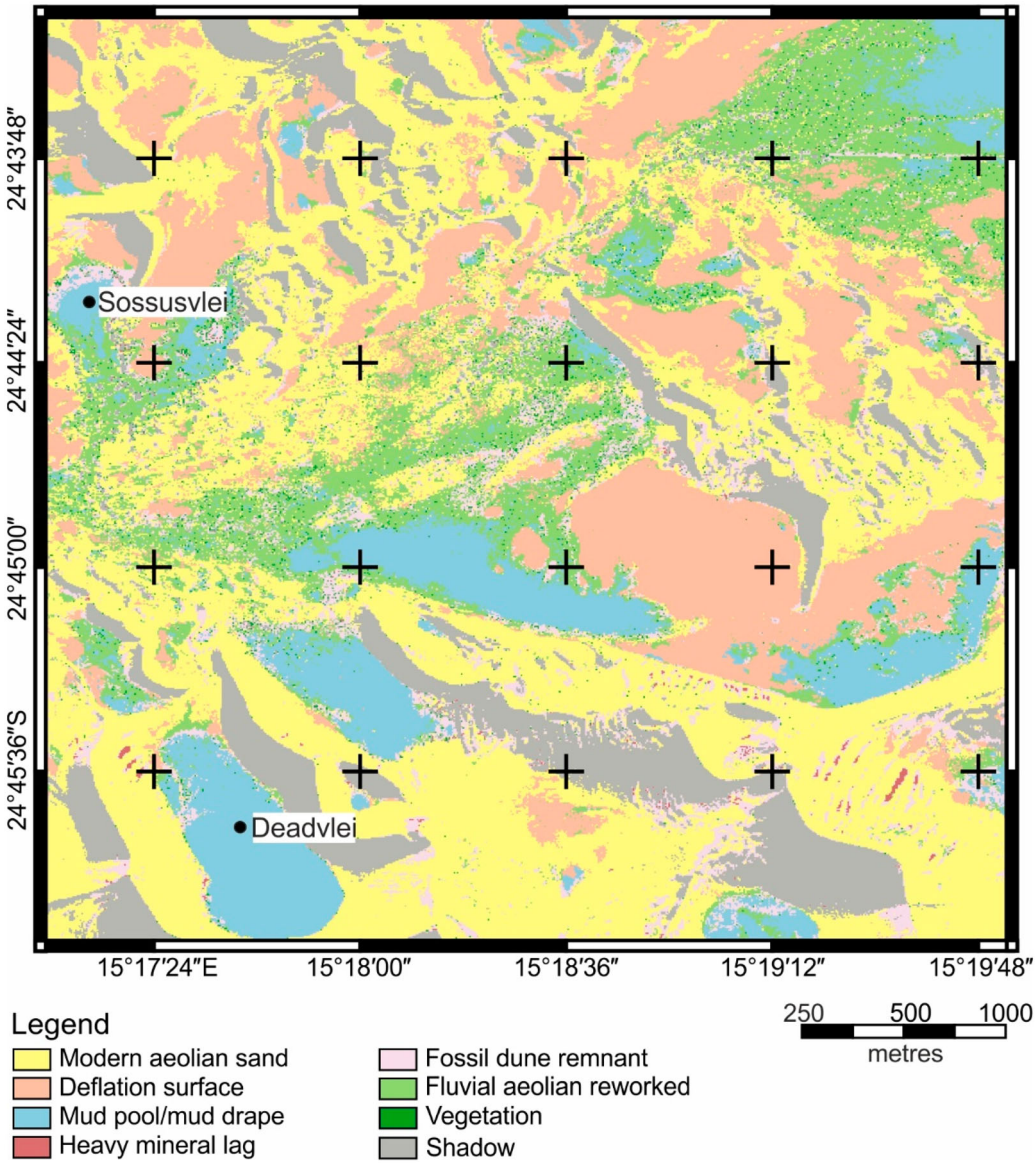

Figure 6. The facies map displays the output of the supervised random forest classification trained with field observations, a combination of Principal Component Analysis, band ratios, texture and geomorphologic indices. Masks were applied for vegetation and shadows. The facies show a complex distribution pattern. Modern aeolian sand occurs on the steep dunes and on sand sheets. Bypass surfaces develop in inter-dune areas, but also on the slightly inclined dune bases. Mud pools build 'vleis' in inter-dune areas, where the river was dammed by the dunes. Mud drapes can be found around the thalweg. On the southern part of the map heavy mineral lags accumulate on the dune flanks. Fossil dune remnants are exposed directly next to the vleis and fluvial–aeolian reworked sediments accumulate adjacent to mud pools (Image © 2015 DigitalGlobe, Inc.).

In the classification for fluvial–aeolian interactions in desert-margin settings (Al-Masrahy & Mountney, 2015), the Sossusvlei area can be classified as 'Termination of fluvial channel network in Aeolian dune fields'. The interaction is fully aeolian dominant (Liu & Coulthard, 2015) as the river flows only very sporadically (Brook et al., 2006) and the reworking of the deposits starts immediately.

5. Conclusions

The detailed map of Sossusvlei presented here highlights the distribution and diversity of sedimentary facies resulting from the interplay of fluvial and aeolian processes in a hyperarid desert environment. The results obtained allowed us to propose a workflow suitable to differentiate and classify facies in fluvio-aeolian environments by the efficient use of remote sensing techniques. Modern aeolian sand and mud pool/mud drape facies can be discriminated with the highest degree of confidence using solely spectral data. Other facies are closer in composition and they can be discriminated only by integrating textural and geomorphological constraints (based on using GLCM from remote sensing spectra for textural analysis and DEM data to extract slope and TPI data). Sedimentological ground-truthing is essential to validate the remote-sensed map. Remote sensing analysis is advantageous over other techniques concerning the scale of mapping and accessibility of the area.

The integrated mapping of mineralogical, textural, and geomorphological parameters can provide a greater level of detail into accurately mapping land surface sedimentary facies and through this provide important insights into sedimentological processes in dryland environments. Fossil dune remnants are exposed through fluvial erosion. Mud pools are abraded and small mud chips accumulate on dune flanks. Fluvial sand deposits are immediately aeolian reworked and mixed with aeolian sand. Course fluvial material is redistributed during high wind energy events and accumulates on deflation surfaces between the dunes.

The remote sensing approach is proven to be a helpful tool for successfully mapping sedimentary facies in the Namib Desert, an essential step to study dune-river interactions in arid environments. With a better understanding of spatial facies distribution, ancient desert environments can be reconstructed more accurately and 'desertification' processes monitored more precisely. The same combination of methods applied here can enable mapping of sedimentary facies on other planets.

Software

All the pre-processing of the satellite image was done in R studio, using R language. Morphological indices like TPI and slope were calculated using the TecGEM toolbox, which is python-based and still under development. All processing is also conducted in R language (R Core Team, 2016) using the packagers raster (Hijmans, 2017), rgdal (Bivand et al., 2017), glcm (Zvoleff, 2016) and randomForest (Liaw et al., 2015). The map was created in Quantum GIS and later augmented with Corel Draw X7.

Acknowledgements

We would like to thank the Geological Survey of Namibia, especially Anna Nguno for all her help with the preparation of field work logistics. Permission and support to work in the area by the Ministry of Environment and Tourism and the game wardens of the Namib-Naukluft Park are gratefully acknowledged. Special thanks to the Helmholtz Institute Freiberg for Resource Technology, Division 'Exploration Technology" for discussion and access to the optical spectroscopy laboratory.

Disclosure statement

No potential conflict of interest was reported by the authors.

ORCID

Robert Zimmermann http://orcid.org/0000-0001-6200-2704
Harald Stollhofen http://orcid.org/0000-0002-2782-3440
Luca Caracciolo http://orcid.org/0000-0001-5275-9834
Eduardo Garzanti http://orcid.org/0000-0002-8638-9322
Louis Andreani http://orcid.org/0000-0002-5916-155X

References

Al-Masrahy, M. A., & Mountney, N. P. (2015). A classification scheme for fluvial–aeolian system interaction in desert-margin settings. *Aeolian Research*, *17*, 67–88. doi:10.1016/j.aeolia.2015.01.010

Amer, R., Kusky, T., & Ghulam, A. (2010). Lithological mapping in the Central Eastern Desert of Egypt using ASTER data. *Journal of African Earth Sciences*, *56*(2-3), 75–82. doi:10.1016/j.jafrearsci.2009.06.004

Andreani, L., Stanek, K., Gloaguen, R., Krentz, O., & Domínguez-González, L. (2014). DEM-based Analysis of interactions between tectonics and landscapes in the ore mountains and Eger Rift (East Germany and NW Czech Republic). *Remote Sensing*, *6*(9), 7971–8001. doi:10.3390/rs6097971

Barber, D. G., & LeDrew, E. F. (1991). SAR sea Ice discrimination using texture statistics: A multivariate approach. *Photogrammetric Engineering and Remote Sensing*, *57*(4), 385–395.

Bertoldi, L., Massironi, M., Visonà, D., Carosi, R., Montomoli, C., Gubert, F., … Pelizzo, M. G. (2011). Mapping the buraburi granite in the himalaya of western Nepal: Remote sensing analysis in a collisional belt with vegetation cover and extreme variation of topography. *Remote Sensing of Environment*, *115*(5), 1129–1144. doi:10.1016/j.rse.2010.12.016

Besler, H. (1980). *Die Dünen-Namib: Entstehung und Dynamik eines Ergs*. Stuttgart: Stuttgarter Geographische Studien. 208 pp.

Bivand, R., Keitt, T., Rowlingson, B., Pebesma, E., Sumner, M., Hijmans, R., & Rousault, E. (2017). rgdal: Bindings for the 'Geospatial' Data Abstraction Library. http://www.gdal.org, https://r-forge.r-project.org/projects/rgdal/

Blumberg, D. G. (2006). Analysis of large aeolian (wind-blown) bedforms using the Shuttle Radar Topography Mission (SRTM) digital elevation data. *Remote Sensing of Environment*, *100*, 179–189. doi:10.1016/j.rse.2005.10.011

Breed, C. S., Fryberger, S. G., Andrews, S., McCauley, C., Lennartz, F., Gebel, D., & Horstman, K. (1979). Regional studies of sand seas using landsat (ERTS) imagery. In E. D. McKee (Ed.), *A study of global sand seas* (pp. 253–304). Washington, DC: U.S. Government Printing Office.

Breiman, L. (2001). Random forests. *Machine Learning*, *45*, 5–32.

Brook, G. A., Srivastava, P., & Marais, E. (2006). Characteristics and OSL minimum ages of relict fluvial deposits near Sossus Vlei, Tsauchab River, Namibia, and a regional climate record for the last 30?: Ka. *Journal of Quaternary Science*, *21*(4), 347–362. doi:10.1002/jqs.977

Bullard, J. E., & Livingstone, I. (2002). Interactions between aeolian and fluvial systems in dryland environments. *Area*, *34*(1), 8–16. doi:10.1111/1475-4762.00052

Bullard, J. E., White, K., & Livingstone, I. (2011a). Morphometric analysis of aeolian bedforms in the Namib Sand Sea using ASTER data. *Earth Surface Processes and Landforms*, *36*, 1534–1549.

Bullard, J. E., White, K., & Livingstone, I. (2011b). Morphometric analysis of aeolian bedforms in the Namib Sand Sea using ASTER data. *Earth Surface Processes and Landforms*, *36*(11), 1534–1549. doi:10.1002/esp.2189

Castañeda, C., Herrero, J., & Casterad, M. A. (2005). Facies identification within the playa-lakes of the Monegros desert, Spain, from field and satellite data. *CATENA*, *63*(1), 39–63. doi:10.1016/j.catena.2005.05.011

Chavez, P. S. (1988). An improved dark-object subtraction technique for atmospheric scattering correction of multispectral data. *Remote Sensing of Environment*, *24*(3), 459–479. doi:10.1016/0034-4257(88)90019-3

Cracknell, M. J., & Reading, A. M. (2014). Geological mapping using remote sensing data: A comparison of five machine learning algorithms, their response to variations in the spatial distribution of training data and the use of explicit spatial information. *Computers & Geosciences*, *63*, 22–33. doi:10.1016/j.cageo.2013.10.008

Cudahy, T., Jones, M., Thomas, M., Laukamp, C., Caccetta, M., Hewson, R., … Verall, M. (2008). Next Generation Mineral Mapping: Queensland Airborne Hymap and Satellite ASTER Surveys 2006-2006. *CSIRO Exploration & Mining Report, P2007 / 364*.

Digital Globe. Data Sheet WorldView-3. Retrieved from https://www.spaceimagingme.com/downloads/sensors/datasheets/DG_WorldView3_DS_2014.pdf

Eckardt, F. D., Soderberg, K., Coop, L. J., Muller, A. A., Vickery, K. J., Grandin, R. D., … Henschel, J. (2013). The nature of moisture at Gobabeb, in the central Namib Desert. *Journal of Arid Environments*, *93*, 7–19. doi:10.1016/j.jaridenv.2012.01.011

Elsayed Zeinelabdein, K. A., & Albiely, A. I. (2008). Ratio image processing techiques: A prospecting tool for mineral deposits, Red Sea Hills, NE Sudan. *The International Archives of the Photogrammetry, Remote Sensing and Spatial Information*, *37*(B8), 1295–1297.

Fryberger, S. G., Krystinik, L. F., & Schenk, C. J. (1990). Modern and ancient eolian deposits: Hydrocarbon exploration and production. *Society of Economic Paleontologists and Mineralogists Rocky Mountain Section*, *5*, 1–11.

Gad, S., & Kusky, T. (2007). ASTER spectral ratioing for lithological mapping in the Arabian–Nubian shield, the Neoproterozoic Wadi kid area, Sinai, Egypt. *Gondwana Research*, *11*(3), 326–335. doi:10.1016/j.gr.2006.02.010

Gallant, J., & Wilson, J. (2000). *Terrain analysis: Principles and applications: Primary topographic attributes*. New York, NY: Wiley.

Garzanti, E., Andò, S., Vezzoli, G., Lustrino, M., Boni, M., & Vermeesch, P. (2012). Petrology of the Namib Sand Sea: Long-distance transport and compositional variability in the wind-displaced Orange Delta. *Earth-Science Reviews*, *112*(3–4), 173–189. doi:10.1016/j.earscirev.2012.02.008

Garzanti, E., Dinis, P., Vermeesch, P., Andò, S., Hahn, A., Huvi, J., … Lancaster, N. (2017). Sedimentary processes controlling ultralong cells of littoral transport: Placer formation and termination of the Orange sand highway in southern Angola. *Sedimentology*, *4*, 597. doi:10.1111/sed.12387

Garzanti, E., Resentini, A., Andò, S., Vezzoli, G., Pereira, A., Vermeesch, P., & Lancaster, N. (2015). Physical controls on sand composition and relative durability of detrital minerals during ultra-long distance littoral and aeolian transport (Namibia and southern Angola). *Sedimentology*, *62*(4), 971–996. doi:10.1111/sed.12169

Gitelson, A., & Merzlyak, M. N. (1994). Spectral reflectance changes associated with autumn senescence of *Aesculus hippocastanum* L. and *Acer platanoides* L. Leaves: Spectral features and relation to chlorophyll estimation. *Journal of Plant Physiology*, *143*, 286–292.

Gomez, C., Delacourt, C., Allemand, P., Ledru, P., & Wackerle, R. (2005). Using ASTER remote sensing data set for geological mapping, in Namibia. *Physics and Chemistry of the Earth, Parts A/B/C*, *30*(1–3), 97–108. doi:10.1016/j.pce.2004.08.042

Haralick, R. M., Shanmugam, K., & Dinstein, I. (1973). Textural features for image classification. *IEEE Transactions on Systems, Man and Cybernetics*, *SMC-3*, 610–621.

Henrich, V., Krauss, G., Götze, C., & Sandow, C. (2017). Index Database: A database for remote sensing indices. Retrieved from https://www.indexdatabase.de/db/ias.php

Hijmans, R. J. (2017). raster: Geographic Data Analysis and Modeling. R package version 2.6-7. https://CRAN.R-project.org/package=raster

Hunt, G. R. (1977). Spectral signatures of particulate minerals in the visible and near infrared. *GEOPHYSICS*, *42*(3), 501–513. doi:10.1190/1.1440721

Jacobson, P., Jacobson, K., & Seely, M. (1995). Ephemeral rivers and their catchments: Sustaining People and Development in Western Namibia. *Desert Research Foundation of Namibia, Windhoek*, 160pp.

Krapf, C. B. E., Stollhofen, H., & Stanistreet, I. G. (2003). Contrasting styles of ephemeral river systems and their interaction with dunes of the Skeleton Coast erg (Namibia). *Quaternary International*, *104*(1), 41–52. doi:10.1016/S1040-6182(02)00134-9

Kruse, F., Baugh, W., & Perry, S. (2015). Validation of DigitalGlobe WorldView-3 Earth imaging satellite shortwave infrared bands for mineral mapping. *Journal of Applied Remote Sensing*, *9*(1). doi:10.1117/1.JRS.9.096044

Kruse, F. A., & Perry, S. L. (2013). Mineral mapping using simulated worldview-3 short-wave-infrared imagery. *Remote Sensing*, *5*(6), 2688–2703. doi:10.3390/rs5062688

Kuester, M. (2016). Radiometric Use of WorldView-3 Imagery. Retrieved from https://dg-cms-uploads-production.s3.amazonaws.com/uploads/document/file/207/Radiometric_Use_of_WorldView-3_v2.pdf

Lancaster, N. (1985). Winds and sand movements in the Namib Sand Sea. *Earth Surface Processes and Landforms*, *10*, 607–619.

Lancaster, N. (1989). *Then Namib Sand Sea: Dune forms, processes and sediments*. Rotterdam: Balkema.

Lancaster, N. (2002). How dry was dry? Late Pleistocene palaeoclimates in the Namib Desert. *Quaternary Science Reviews*, *21*(7), 769–782. doi:10.1016/S0277-3791(01)00126-3

Lancaster, N. (2014). Dune systems of the Namib Desert – a spatial and temporal perspective. *Transactions of the Royal Society of South Africa*, *69*(3), 133–137. doi:10.1080/0035919X.2014.924085

Lancaster, N., & Teller, J. T. (1988). Interdune deposits of the Namib Sand Sea. *Sedimentary Geology*, *55*(1-2), 91–107. doi:10.1016/0037-0738(88)90091-7

Langford, R. P. (1989). Fluvial-aeolian interactions: Part I, modern systems. *Sedimentology*, *36*, 1023–1035.

Lass, H. U., Schmidt, M., Mohrholz, V., & Nausch, G. (2000). Hydrographic and current measurements in the area of the Angola–Benguela front. *Journal of Physical Oceanography*, *30*(10), 2589–2609. doi:10.1175/1520-0485(2000)030<2589:HACMIT>2.0.CO;2

Liaw, A., Wiener, M., Breiman, L., & Cutler, A. (2015). randomForest: Breiman and Cutler's Random Forests for Classification and Regression. https://www.stat.berkeley.edu/~breiman/RandomForests/

Liu, B., & Coulthard, T. J. (2015). Mapping the interactions between rivers and sand dunes: Implications for fluvial and aeolian geomorphology. *Geomorphology*, *231*, 246–257. doi:10.1016/j.geomorph.2014.12.011

Livingstone, I. (2013). Aeolian geomorphology of the Namib Sand Sea. *Journal of Arid Environments*, *93*, 30–39. doi:10.1016/j.jaridenv.2012.08.005

Livingstone, I., Bristow, C., Bryant, R. G., Bullard, J., White, K., Wiggs, G. F. S., … Thomas, D. S. G. (2010). The Namib Sand Sea digital database of aeolian dunes and key forcing variables. *Aeolian Research*, *2*(2–3), 93–104. doi:10.1016/j.aeolia.2010.08.001

Maeder, J., Narumalani, S., Rundquist, D., Perk, R., Schalles, J., Hutchins, K., & Keck, J. (2002). Classifying and mapping general coral-reef structure using Ikonos data. *Photogrammetric Engineering and Remote Sensing*, *68*(12), 1297–1305.

Miller, R. M., & Becker, T. (2008). *The geology of Namibia*. Windhoek: Ministry of Mines and Energy.

Parker, T. J., Gorsline, D. S., Saunders, R. S., Pieri, D. C., & Schneeberger, D. M. (1993). Coastal geomorphology of the Martian northern plains. *Journal of Geophysical Research: Planets*, *98*(E6), 11061. doi:10.1029/93JE00618

Quintanar, J., Khan, S. D., Fathy, M. S., & Zalat, A.-F. A. (2013). Remote sensing, planform, and facies analysis of the Plain of Tineh, Egypt for the remains of the defunct Pelusiac River. *Sedimentary Geology*, *297*, 16–30. doi:10.1016/j.sedgeo.2013.09.002

Raines, G. L., Offield, T. W., & Santos, E. S. (1978). Remote-sensing and subsurface definition of facies and structure related to uranium deposits, Powder River basin, Wyoming. *Economic Geology*, *73*(8), 1706–1723. doi:10.2113/gsecongeo.73.8.1706

R Core Team. (2016). *R: A language and environment for statistical*. Vienna: R Foundation for Statistical Computing. https://www.R-project.org

Richards, D. L., Schreiber, U. M., Tjikukutu, G., & Cloete, S. P. (Cartographers). (2000). *Geological Map of Namibia, 1:250 000 geological series, sheet 2414 - Meob Bay*. Windhoek: Ministry of Mines and Energy.

Rogers, J. (1977). *Sedimentation on the continental margin off the Orange River and the Namib Desert* (Joint Geological Survey/University of Cape Town Marine Geoscience Group, Trans.). Department of Geology, University of Cape Town.

Rosenqvist, A., Shimada, M., & Watanabe, M. (2004). ALOS PALSAR: Technical outline and mission concepts. *International Symposium on Retrieval of Bio- and Geophysical Parameters from SAR Data for Land Applications*, *1*(7), 1–7.

Roskin, J., Bookman, R., Friesem, D. E., & Vardi, J. (2017). A late Pleistocene linear dune dam record of aeolian-fluvial dynamics at the fringes of the northwestern Negev dunefield. *Sedimentary Geology*, *353*, 76–95. doi:10.1016/j.sedgeo.2017.03.011

Rowan, L. C., & Mars, J. C. (2003). Lithologic mapping in the Mountain Pass, California area using Advanced Spaceborne Thermal Emission and Reflection Radiometer (ASTER) data. *Remote Sensing of Environment*, *84*(3), 350–366. doi:10.1016/S0034-4257(02)00127-X

Rowell, A., Thomas, D., Bailey, R., Stone, A., Garzanti, E., & Padoan, M. (2018). Controls on sand ramp formation in southern Namibia. *Earth Surface Processes and Landforms*, *43*(1), 150–171. doi:10.1002/esp.4159

Sabins, F. F. (1999). Remote sensing for mineral exploration. *Ore Geology Reviews*, *14*(3–4), 157–183. doi:10.1016/S0169-1368(99)00007-4

Shannon, L. V., Boyd, A. J., Brundrit, G. B., & Taunton-Clark, J. (1986). On the existence of an El Niño-type phenomenon in the Benguela System. *Journal of Marine Research*, *44*(3), 495–520. doi:10.1357/002224086788403105

Shannon, L. V., & Nelson, G. (1996). The Benguela: Large scale features and processes and system variability. In *The south atlantic* (pp. 163–210). Berlin, Heidelberg: Springer.

Stanistreet, I. G., & Stollhofen, H. (2002). Hoanib river flood deposits of namib desert interdunes as analogues for thin permeability barrier mudstone layers in aeolianite reservoirs. *Sedimentology*, *49*(4), 719–736. doi:10.1046/j.1365-3091.2002.00458.x

Stepinski, T. F., Collier, M. L., McGovern, P. J., & Clifford, S. M. (2004). Martian geomorphology from fractal analysis of drainage networks. *Journal of Geophysical Research: Planets*, *109*(E2), 1–12. doi:10.1029/2003JE002098

Stone, A. E. C. (2013). Age and dynamics of the Namib Sand Sea: A review of chronological evidence and possible landscape development models. *Journal of African Earth Sciences*, *82*, 70–87. doi:10.1016/j.jafrearsci.2013.02.003

Strohbach, B. J. (2008). Mapping the major catchments of namibia. *Agricola*, *18*, 63–73.

Telfer, M. W., Parteli, E. J., Radebaugh, J., Beyer, R. A., Bertrand, T., Forget, F., … Spencer, J. (2018). Dunes on Pluto. *Science*, *360*, 992–997.

van der Meer, F. D., Bakker, W. H., Scholte, K., Skidmore, A., de Jong, S., Clevers, J., & Epema, G. (2000). Vegetation indices, above ground biomass estimates and the red edge from Meris. *International Archives of Photogrammetry and Remote Sensing*, *XXXIII*(B7), 1580–1587.

van der Meer, F. D., van der Werff, H. M. A., van Ruitenbeek, F. J. A., Hecker, C. A., Bakker, W. H., Noomen, M. F., …

Woldai, T. (2012). Multi- and hyperspectral geologic remote sensing: A review. *International Journal of Applied Earth Observation and Geoinformation*, *14*(1), 112–128. doi:10.1016/j.jag.2011.08.002

Villers, J. d., Wiid, B. L., Kleywegt, R. J., Martin, H., Heath, D. C., & Besaans, A. J. (Bouguer Anomalies). (1964). *Geological Map of south-West Africa. Showing mineral occurrences and gravity contours*. (Cartographers). Pretoria: The Government and Stationery Office. The Republic of South Africa, Pretoria and Cape Town.

Walden, J., White, K., & Drakes, N. A. (1996). Controls on dune colour in the Namib sand sea: Preliminary results. *Journal of African Earth Sciences*, *22*(3), 349–353.

Ward, J. D. (1988). Eolian, fluvial and pan (playa) facies of the Tertiary Tsondab Sandstone formation in the central Namib Desert, Namibia. *Sedimentary Geology*, *55*(1-2), 143–162. doi:10.1016/0037-0738(88)90094-2

White, K., Walden, J., & Gurney, S. D. (2007). Spectral properties, iron oxide content and provenance of Namib dune sands. *Geomorphology*, *86*(3–4), 219–229. doi:10.1016/j.geomorph.2006.08.014

Ye, B., Tian, S., Ge, J., & Sun, Y. (2017). Assessment of WorldView-3 data for lithological mapping. *Remote Sensing*, *9*(11), 1132. doi:10.3390/rs9111132

Zaini, N., van der Meer, F., & van der Werff, H. (2014). Determination of carbonate rock chemistry using laboratory-based hyperspectral imagery. *Remote Sensing*, *6*(12), 4149–4172. doi:10.3390/rs6054149

Zimmermann, R., Brandmeier, M., Andreani, L., Mhopjeni, K., & Gloaguen, R. (2016). Remote sensing exploration of Nb-Ta-LREE-enriched carbonatite (epembe/Namibia). *Remote Sensing*, *8*(8), 620. doi:10.3390/rs8080620

Zvoleff, A. (2016). glcm: Calculate Textures from Grey-Level Co-Occurrence Matrices (GLCMs). http://www.azvoleff.com/glcm